J. Appl. Comput. Mech., 10(2) (2024) 272-286
DOI: 10.22055/jacm.2023.44690.4259

ISSN: 2383-4536
jacm.scu.ac.ir

Shahid Chamran University of Ahvaz

Journal of Applied and Computational Mechanics

Research Paper

Unsteady Meshfree Framework for Double-diffusive Natural Convection with Boundary and Geometry Effects

Judy P. Yang, I-Ting Liao

Department of Civil Engineering, National Yang Ming Chiao Tung University, Hsinchu 300093, Taiwan,
Email: jpyang@nycu.edu.tw (J.P.Y.); sweet16love930340@gmail.com (I.T.L.)

Received September 02 2023; Revised October 30 2023; Accepted for publication October 31 2023.
Corresponding author: J.P. Yang (jpyang@nycu.edu.tw)

Abstract. In this study, a meshfree framework based on the reproducing kernel collocation method is proposed for incremental-iterative analysis of double-diffusive natural convection in a porous enclosure, in which the forward difference method is adopted for temporal discretization, and the two-step version of Newton-Raphson method is used for iteration. As the double-diffusive convection problem is composed of multi phases and is influenced by both material and geometric parameters, the resulting system is highly nonlinear and complicated. From the numerical investigation, the partially heated boundary with different buoyancy ratios can yield monocellular flow problems with opposite phenomena depending on the contribution of thermal/solute buoyancy force. For the domains with burrowing inside, the key feature is the contour of stream function, which is separated into two vortexes by the hole in the simply connected domain while the two vortexes are not separated completely in the multiply connected domain due to the geometric compression of two holes. It is further shown that the framework is capable of solving various double-diffusive convection problems with satisfactory accuracy and efficiency by uniform discretization as well as few source points in the approximation.

Keywords: Reproducing kernel collocation; double-diffusive; natural convection; phase coupling; unsteady state.

1. Introduction

The investigation of double-diffusive natural convection in porous media has begun mainly in 1970s [1]. Since then, more attention has been drawn in virtue of its wide applications in the process of chemical vapor transport and in the development of methods for crystal growth of alloys or semi-conductors [2]. As there exist numerous factors affecting the behavior of double-diffusive natural convection, the research direction of double-diffusive convection has moved from heat transfer to heat and mass transfer as caused by both temperature and concentration gradients. More complicated environment with special fluid was further considered, for instance, the double-diffusive convection in a nanofluid layer [3] and the effect of the magnetic field inclination on double-diffusive convection [4]. Furthermore, it is found that the governing equations of various systems can be established by using a similar concept (e.g., balance laws) while the terms included in the governing equations may be quite different due to the assumptions made in the derivation, indicating the complexity of double-diffusive convection.

With the prosperous development of computational methods, the double-diffusive natural convection in a fluid-saturated porous medium is numerically studied to particularly investigate the influences of certain parameters and their effects. Based on Darcy's law, for a rectangular enclosure in the downward gravitational field [2, 5], the two-dimensional analysis was conducted, to name but a few in the following. The finite element method was adopted for spatial discretization while the finite difference method, Crank-Nicolson scheme, was used for temporal discretization, in which the effect of buoyancy ratio between temperature and concentration was of major concern [2]. The finite difference method was introduced for spatial discretization and the central difference method was used for temporal discretization, in which the effects of heat generation or absorption were of interests [5]. Recently, an upwind compact difference scheme for spatial discretization with the fourth-order Runge-Kutta method for temporal discretization was proposed for double-diffusive convection, with focus on the aspect ratio of the rectangular cavity [6]. A Darcy-Brinkman formulation is proposed to solve the double-diffusive natural convection problem by using the finite volume approach [7]. A three-dimensional numerical analysis was conducted to simulate the double-diffusive process in a rectangular cavity by using the stabilized finite element method to overcome the predominantly advection problem considering a series of buoyancy ratios and fluid parameters [8]. In another work, the double-diffusive natural convection in an inclined enclosure is studied by the hybrid lattice Boltzmann-finite difference method, where the Navier-Stokes equations were adopted as the heat and mass transfer model to include the heat generation and Soret effect [9]. From these studies, advanced numerical methods are urgent for unveiling the phenomena of double-diffusive convection.

Unlike the above weak form-based methods as commonly adopted in conjunction with the models of computational fluid dynamics for analyzing complicated problems or phenomena by commercial software [10], to avoid background mesh for

Published online: November 08 2023

computational efficiency, the present study focuses on the development of an effective numerical framework using the meshfree strong-form methods [11-14]. In the literature, for a fluid-saturated porous enclosure, the steady-state equations have been investigated by the local RBF collocation method [15], generalized finite difference method (GFDM) [16], and reproducing kernel collocation method (RKCM) [17,18]. The local nature of approximation in the aforementioned meshfree methods was shown to be effective and efficient in solving the above steady-state problems involving two-phase variables (stream function and temperature) or three-phase variables (stream function, temperature, and concentration). Recently, the unsteady-state double-diffusive convection problems were further untangled by the strong-form meshfree methods. The space-time generalized finite difference method [19] was proposed to deal with the three-phase coupling problem. By considering the continuity equation in addition to the above three governing equations, a four-phase coupling problem involving vorticity is further established. RKCM with a time integration scheme [20] was recently proposed to solve this unsteady-state double-diffusive convection problem. Since the space-time GFDM treats time as the spatial coordinate, the collocation points discretized along the time axis might require more points to ensure accuracy in solving the unsteady-state equations. In view of the expansive dimension adopted in the solution process, based on the previous work [20], the Newton-Raphson collocation method in conjunction with the reproducing kernel approximation is adopted in this study, which will turn out to be more efficient than the space-time method when the forward difference method is adopted for temporal discretization.

For the double-diffusive natural convection in a parallelogram, two different boundary conditions are classified, the combined global heat and mass flows as well as the opposite global heat and mass flows, which were discussed using the steady-state equations in the literature [18]. In this study, both boundary conditions will be further investigated by considering the unsteady-state responses. Additionally, more complicated boundary and domain geometry are to be investigated. The structure of this study is described as follows: The mathematical formulation of the three-phase coupling nonlinear system is presented in Section 2. The collocation framework including the forward difference method and Newton-Raphson method is introduced in Section 3. The numerical investigation is given in Section 4. Section 5 concludes this study.

2. Mathematical Formulation

2.1. Unsteady-state double-diffusive natural convection

As depicted in Fig. 1, a two-dimensional rectangular domain has sides of length L and H with an inclined angle θ in the field of gravitation g. In this unsteady-state physical problem, a fluid-saturated porous medium is assumed [21], in which the enclosure is regarded as the perfectly isotropic mixture with incompressible and laminar Newtonian-fluid inside [22]. It should be noted that Soret effect or the thermal-diffusion effect is a coupled process of mass flow due to a temperature gradient, while Dufour effect or the diffusion-thermal effect is a coupled process of heat flow caused by a concentration gradient. Since these effects are of quite small magnitudes in the two-component fluid mixture, they are mostly neglected in heat and mass transfer problems [21, 23].

The double-diffusive natural convection is described in a porous enclosure based on the continuity, balance laws of momentum, thermal energy, and concentration in the dimensional form as follows:

$$\frac{\partial u}{\partial X}+\frac{\partial v}{\partial Y}=0 \tag{1}$$

$$\frac{\partial^2\phi}{\partial X^2}+\frac{\partial^2\phi}{\partial Y^2}+\frac{g\beta_T\rho L^2}{\nu}\frac{\partial\vartheta}{\partial X}+\frac{g\beta_C\rho L^2}{\nu}\frac{\partial c}{\partial X}=0 \tag{2}$$

$$\frac{\partial\vartheta}{\partial\tau}+u\frac{\partial\vartheta}{\partial X}+v\frac{\partial\vartheta}{\partial Y}=\alpha_e\left(\frac{\partial^2\vartheta}{\partial X^2}+\frac{\partial^2\vartheta}{\partial Y^2}\right) \tag{3}$$

$$\frac{\partial c}{\partial\tau}+u\frac{\partial c}{\partial X}+v\frac{\partial c}{\partial Y}=D\left(\frac{\partial^2 c}{\partial X^2}+\frac{\partial^2 c}{\partial Y^2}\right) \tag{4}$$

where u and v are the components of velocity in the X and Y directions, respectively; ϕ, ϑ, and c are the field variables in the time domain τ, including the stream function, temperature, and concentration. The rest parameters are described below [8]: β_T and β_C are the coefficients of thermal and compositional expansion, respectively; ρ and ν are the density and kinematic viscosity of the fluid; α_e is the effective thermal diffusivity of the porous medium; D is the species diffusivity. The boundary conditions will be detailed after normalization as given in Section 2.3.

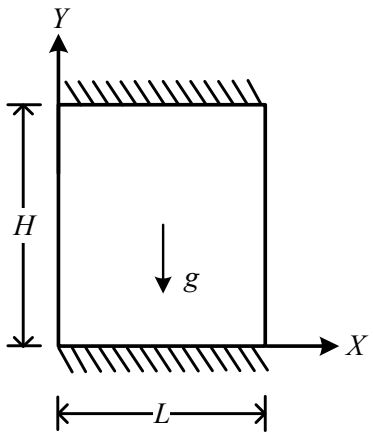

Fig. 1. Physical model of the porous enclosure.

2.2. Mathematical model in dimensionless form

To compare with the numerical results existing in the literature and reduce the numbers of field variables and material parameters, the aforementioned equations are normalized. The following dimensionless coordinates and variables are defined:

$$x=\frac{X}{L},\ y=\frac{Y}{L},\ t=\frac{\alpha_e \tau}{L^2} \tag{5}$$

$$\psi=\frac{\phi}{\rho\alpha_e},\ T=\frac{\vartheta-\vartheta_l}{\vartheta_h-\vartheta_l},\ C=\frac{c-c_l}{c_h-c_l},\ U=\frac{uL}{\alpha_e},\ V=\frac{vL}{\alpha_e} \tag{6}$$

where ϑ_h and c_h denote the higher values of ϑ and c; ϑ_l and c_l denote the lower values of ϑ and c. By adopting the scale-based analysis and introducing Eqs. (5)-(6) to Eqs. (1)-(4), the following equations can be derived:

$$\frac{\partial U}{\partial x}+\frac{\partial V}{\partial y}=0 \tag{7}$$

$$\frac{\partial^2\psi}{\partial x^2}+\frac{\partial^2\psi}{\partial y^2}+Ra\left(\frac{\partial T}{\partial x}+N\frac{\partial C}{\partial x}\right)=0 \tag{8}$$

$$\frac{\partial T}{\partial t}+\frac{\partial (UT)}{\partial x}+\frac{\partial (VT)}{\partial y}-\left(\frac{\partial^2 T}{\partial x^2}+\frac{\partial^2 T}{\partial y^2}\right)=0 \tag{9}$$

$$\frac{\partial C}{\partial t}+\frac{\partial (UC)}{\partial x}+\frac{\partial (VC)}{\partial y}-\frac{1}{Le}\left(\frac{\partial^2 C}{\partial x^2}+\frac{\partial^2 C}{\partial y^2}\right)=0 \tag{10}$$

From the normalized continuity equation given in Eq. (7), the normalized stream function ψ can be introduced through Darcy's law:

$$U=\frac{\partial\psi}{\partial y},\ V=-\frac{\partial\psi}{\partial x} \tag{11}$$

After substituting Eq. (11) into Eqs. (9)-(10), the following governing equations involving three variables are reached:

$$\nabla^2\psi+Ra\left(\frac{\partial T}{\partial x}+N\frac{\partial C}{\partial x}\right)=0 \tag{12}$$

$$\frac{\partial T}{\partial t}+\frac{\partial\psi}{\partial y}\frac{\partial T}{\partial x}-\frac{\partial\psi}{\partial x}\frac{\partial T}{\partial y}-\nabla^2 T=0 \tag{13}$$

$$\frac{\partial C}{\partial t}+\frac{\partial\psi}{\partial y}\frac{\partial C}{\partial x}-\frac{\partial\psi}{\partial x}\frac{\partial C}{\partial y}-\frac{1}{Le}\nabla^2 C=0 \tag{14}$$

where ψ, T, and C are the dimensionless stream function, temperature, and concentration. The above equations correspond to the normalized momentum, normalized energy, and normalized concentration (or solute). The rest dimensionless parameters are defined as [18]:

$$Ra=\frac{g\beta_T(\theta_h-\theta_l)L^3}{\alpha_e\nu},\ Le=\frac{\alpha_e}{D},\ N=\frac{\beta_C(c_h-c_l)}{\beta_T(\theta_h-\theta_l)} \tag{15}$$

in which Ra and Le are the dimensionless Rayleigh number and Lewis number related to the fluid motion accounting for convection effect and diffusion effect, respectively. N is the buoyancy ratio accounting for the driven effect of the solute and thermal buoyancy forces.

2.3. Boundary conditions

In this porous enclosure, the circumference is assumed to be impermeable, i.e., $\psi=0$. For demonstration purpose, a unit square domain is considered. By imposing the Dirichlet boundary conditions of T and C on $x=0$ and $x=1$, the following two types of boundary conditions can be classified:

(1) Combined global heat and mass flows [19]:

$$\begin{aligned}&\psi(0,y)=0,\ T(0,y)=1,\ C(0,y)=1,\\&\psi(1,y)=0,\ T(1,y)=0,\ C(1,y)=0\end{aligned} \tag{16}$$

(2) Opposite global heat and mass flows [18]:

$$\begin{aligned}&\psi(0,y)=0,\ T(0,y)=1,\ C(0,y)=0,\\&\psi(1,y)=0,\ T(1,y)=0,\ C(1,y)=1\end{aligned} \tag{17}$$

The rest boundary conditions along $y=0$ and $y=1$ are listed below [19]:

$$\begin{aligned}&\psi(\mathrm{x},0)=0,\ \frac{\partial T}{\partial \mathrm{y}}(\mathrm{x},0)=0,\ \frac{\partial C}{\partial \mathrm{y}}(\mathrm{x},0)=0,\\&\psi(\mathrm{x},1)=0,\ \frac{\partial T}{\partial \mathrm{y}}(\mathrm{x},1)=0,\ \frac{\partial C}{\partial \mathrm{y}}(\mathrm{x},1)=0\end{aligned} \tag{18}$$

which are insulated (for temperature) and non-diffusive of solute transfer (for concentration). For wider applications, Eq. (18) can be written in the following form for inclined boundary or curved boundary as will be investigated in Section 4:

$$\psi=0,\ \nabla T\cdot\mathbf{n}=0,\ \nabla C\cdot\mathbf{n}=0 \tag{19}$$

where **n** denotes the unit outward normal on the boundary.

2.4. Parameters of heat and mass transfer

Referring to Fig. 1, the average parameters, Nusselt and Sherwood numbers, for the rectangle are defined as follows [24]:

$$Nu=\int_0^H \left.\frac{\partial T}{\partial \mathrm{x}}\right|_{\mathrm{x}=0} d\mathrm{y} \tag{20}$$

$$Sh=\left|\int_0^H \left.\frac{\partial C}{\partial \mathrm{x}}\right|_{\mathrm{x}=0} d\mathrm{y}\right| \tag{21}$$

which are adopted to evaluate the heat and mass flows on the left vertical wall. For the problems in consideration, the average values of Nusselt and Sherwood numbers are computed to compare with the results in the literature in Section 4.

3. Incremental-Iterative Collocation Method

3.1. Forward difference method

For simplicity, the forward difference method is introduced for temporal integration. Then, Eqs. (12)-(14) can be expressed in an incremental form as:

$$\nabla^2\left({}^{\mathrm{t}}\psi\right)+Ra\left[\frac{\partial\left({}^{\mathrm{t}}T\right)}{\partial \mathrm{x}}+N\frac{\partial\left({}^{\mathrm{t}}C\right)}{\partial \mathrm{x}}\right]=0 \tag{22}$$

$${}^{\mathrm{t}+1}T={}^{\mathrm{t}}T+\Delta \mathrm{t}\left[-\frac{\partial\left({}^{\mathrm{t}}\psi\right)}{\partial \mathrm{y}}\frac{\partial\left({}^{\mathrm{t}}T\right)}{\partial \mathrm{x}}+\frac{\partial\left({}^{\mathrm{t}}\psi\right)}{\partial \mathrm{x}}\frac{\partial\left({}^{\mathrm{t}}T\right)}{\partial \mathrm{y}}+\nabla^2\left({}^{\mathrm{t}}T\right)\right] \tag{23}$$

$${}^{\mathrm{t}+1}C={}^{\mathrm{t}}C+\Delta \mathrm{t}\left[-\frac{\partial\left({}^{\mathrm{t}}\psi\right)}{\partial \mathrm{y}}\frac{\partial\left({}^{\mathrm{t}}C\right)}{\partial \mathrm{x}}+\frac{\partial\left({}^{\mathrm{t}}\psi\right)}{\partial \mathrm{x}}\frac{\partial\left({}^{\mathrm{t}}C\right)}{\partial \mathrm{y}}+\frac{1}{Le}\nabla^2\left({}^{\mathrm{t}}C\right)\right] \tag{24}$$

where the superscript t represents an incremental time step. To satisfy the Courant-Friedrichs-Lewy condition, the time increment is set as $\Delta t=10^{-5}$ in this study [20]. To begin the incremental analysis (i.e., $t=0$), the initial conditions of the temperature and concentration should be given while that of the stream function is obtained from Eq. (22).

3.2. Reproducing kernel approximation

The three variables ψ, T, and C in the coupled system are approximated by the reproducing kernel shape function $\Psi_I(\mathbf{x})$ with the following expression:

$$\begin{aligned}\psi(\mathbf{x})&=\sum_{I=1}^{N_s}\Psi_I(\mathbf{x})\,a_I^{\psi}\\T(\mathbf{x})&=\sum_{I=1}^{N_s}\Psi_I(\mathbf{x})\,a_I^{T}\\C(\mathbf{x})&=\sum_{I=1}^{N_s}\Psi_I(\mathbf{x})\,a_I^{C}\end{aligned} \tag{25}$$

where the approximation is established on the N_s source points. In the above equation, a_I^{ψ}, a_I^{T}, and a_I^{C} are the generalized coefficients for each variable. For constructing the reproducing kernel shape function, the selection of monomial basis vector $\mathbf{H}(\mathbf{x}-\mathbf{x}_I)$ of order p and kernel function $\varphi_a(\mathbf{x}-\mathbf{x}_I)$ are required, depending on the problems to be solved [20]:

$$\Psi_I(\mathbf{x})=\mathbf{H}^{\mathrm{T}}(\mathbf{x}-\mathbf{x}_I)\mathbf{b}(\mathbf{x})\varphi_a(\mathbf{x}-\mathbf{x}_I) \tag{26}$$

in which the vector of coefficients $\mathbf{b}(\mathbf{x})$ is determined by the reproducing conditions:

$$\sum_{I=1}^{N_s}\Psi_I(\mathbf{x})\mathbf{x}_I^{\alpha}=\mathbf{x}^{\alpha},\quad 0\le|\alpha|\le p \tag{27}$$

For two-dimensional problems, the multi-index α is defined as $|\alpha|=\alpha_1+\alpha_2$. The general expression of reproducing kernel shape function is:

$$\Psi_I(\mathbf{x})=\mathbf{H}^{\mathrm{T}}(\mathbf{0})\mathbf{M}^{-1}(\mathbf{x})\mathbf{H}(\mathbf{x}-\mathbf{x}_I)\varphi_a(\mathbf{x}-\mathbf{x}_I) \tag{28}$$

with the moment matrix $\mathbf{M}(\mathbf{x})$ given by:

$$\mathbf{M}(\mathbf{x})=\sum_{I=1}^{N_s}\mathbf{H}(\mathbf{x}-\mathbf{x}_I)\mathbf{H}^{\mathrm{T}}(\mathbf{x}-\mathbf{x}_I)\varphi_a(\mathbf{x}-\mathbf{x}_I) \tag{29}$$

Referring to Section 2, the partial differential equations of second-order are to be analyzed. Therefore, the monomial basis vector of $p=2$ and the quintic B-spline kernel function are adopted. For readability, the kernel function is referred to Ref. [20]. It is noted that a circular support of the reproducing kernel shape function is used as described by the support size a. Without loss of generality, $a=(p+\delta)h$ with $\delta>0$ and nodal distance of source points h.

3.3. Reproducing kernel collocation method

In the collocation method, the following three sets of collocation points are defined for the problem:

$$\begin{aligned}\mathbf{x}_p&=\left[\mathbf{x}_{p1},\mathbf{x}_{p2},\ldots,\mathbf{x}_{pN_p}\right]\subseteq\Omega\\ \mathbf{x}_q&=\left[\mathbf{x}_{q1},\mathbf{x}_{q2},\ldots,\mathbf{x}_{qN_q}\right]\subseteq\Gamma_{Neumann}\\ \mathbf{x}_r&=\left[\mathbf{x}_{r1},\mathbf{x}_{r2},\ldots,\mathbf{x}_{rN_r}\right]\subseteq\Gamma_{Dirichlet}\end{aligned} \tag{30}$$

where $\mathbf{x}_p$ denotes the set of collocation points (N_p) in the domain Ω; $\mathbf{x}_q$ denotes the set of collocation points (N_q) on the Neumann boundary $\Gamma_{Neumann}$; $\mathbf{x}_r$ denotes the set of collocation points (N_r) on the Dirichlet boundary $\Gamma_{Dirichlet}$.

The unsteady-state responses are solved incrementally in time, in which the nonlinear iteration is performed at each time step through solving the steady-state parts of the governing equations as given in Eqs. (22)-(24). In the meshfree collocation formulation [25, 26], the reproducing kernel approximation in Eq. (25) is introduced for spatial discretization. Then, the incremental forms of the governing equations are obtained as follows:

$$\sum_{I=1}^{N_s}\left\{\left[\Psi_{I,xx}(\mathbf{x}_{pJ})+\Psi_{I,yy}(\mathbf{x}_{pJ})\right]{}^{\mathrm{t}}a_I^{\psi}+Ra\left[\Psi_{I,x}(\mathbf{x}_{pJ}){}^{\mathrm{t}}a_I^T+\mathrm{N}\Psi_{I,x}(\mathbf{x}_{pJ}){}^{\mathrm{t}}a_I^C\right]\right\}=0 \tag{31}$$

$$\sum_{I=1}^{N_s}\left\{\left[\Psi_{I,xx}(\mathbf{x}_{pJ})+\Psi_{I,yy}(\mathbf{x}_{pJ})\right]{}^{\mathrm{t}}a_I^T-\left[\Psi_{I,y}(\mathbf{x}_{pJ}){}^{\mathrm{t}}a_I^{\psi}\Psi_{I,x}(\mathbf{x}_{pJ}){}^{\mathrm{t}}a_I^T-\Psi_{I,x}(\mathbf{x}_{pJ}){}^{\mathrm{t}}a_I^{\psi}\Psi_{I,y}(\mathbf{x}_{pJ}){}^{\mathrm{t}}a_I^T\right]\right\}=0 \tag{32}$$

$$\sum_{I=1}^{N_s}\left\{\frac{1}{Le}\left[\Psi_{I,xx}(\mathbf{x}_{pJ})+\Psi_{I,yy}(\mathbf{x}_{pJ})\right]{}^{\mathrm{t}}a_I^C-\left[\Psi_{I,y}(\mathbf{x}_{pJ}){}^{\mathrm{t}}a_I^{\psi}\Psi_{I,x}(\mathbf{x}_{pJ}){}^{\mathrm{t}}a_I^C-\Psi_{I,x}(\mathbf{x}_{pJ}){}^{\mathrm{t}}a_I^{\psi}\Psi_{I,y}(\mathbf{x}_{pJ}){}^{\mathrm{t}}a_I^C\right]\right\}=0 \tag{33}$$

As an example, by introducing Eq. (25) to the boundary equations given in Eqs. (16) and (18), the incremental collocation equations on $\Gamma_{Neumann}$ and $\Gamma_{Dirichlet}$ can be derived as follows:

$$\begin{aligned}&\sum_{I=1}^{N_s}\Psi_I(\mathbf{x}_{rJ}){}^{\mathrm{t}}a_I^{\psi}=0\\ &\sum_{I=1}^{N_s}\Psi_I(\mathbf{x}_{rJ}){}^{\mathrm{t}}a_I^T-1=0,\quad\forall x=0\\ &\sum_{I=1}^{N_s}\Psi_I(\mathbf{x}_{rJ}){}^{\mathrm{t}}a_I^C-1=0\end{aligned} \tag{34}$$

$$\begin{aligned}&\sum_{I=1}^{N_s}\Psi_I(\mathbf{x}_{rJ}){}^{\mathrm{t}}a_I^{\psi}=0\\ &\sum_{I=1}^{N_s}\Psi_I(\mathbf{x}_{rJ}){}^{\mathrm{t}}a_I^T=0,\quad\forall x=1\\ &\sum_{I=1}^{N_s}\Psi_I(\mathbf{x}_{rJ}){}^{\mathrm{t}}a_I^C=0\end{aligned} \tag{35}$$

$$\begin{aligned}&\sum_{I=1}^{N_s}\Psi_I(\mathbf{x}_{rJ}){}^{\mathrm{t}}a_I^{\psi}=0\\ &\sum_{I=1}^{N_s}\Psi_{I,y}(\mathbf{x}_{qJ}){}^{\mathrm{t}}a_I^T=0,\quad\forall y=0,1\\ &\sum_{I=1}^{N_s}\Psi_{I,y}(\mathbf{x}_{qJ}){}^{\mathrm{t}}a_I^C=0\end{aligned} \tag{36}$$

where the boundary conditions of combined global heat and mass flows are explicitly given for illustration. Referring to Section 3.1, the initial conditions of the temperature and concentration are given in terms of ${}^0a_I^T$ and ${}^0a_I^C$ (for $I=1,2,\ldots,N_s$) in RKCM.

As there are factors such as interfacial velocities affecting the boundary conditions and yielding a complicated system, Eqs. (16)-(18) are adopted for simplicity by assuming the negligible interfacial velocities [2, 21]. For practical applications, the shape of a parallelogram is considered [2, 21], while the generalization of the formulation (i.e., Eqs. (34)-(36)) can be made if needed.

3.4. Newton-Raphson collocation method

To establish the nonlinear framework, the matrix expression will be adopted in the following for clarity. The governing collocation equations given in Eqs. (31)-(33) are collected as $\mathbf{A}_p$; the Neumann and Dirichlet collocation equations in Eqs. (34)-(36) are collected as $\mathbf{A}_q$ and $\mathbf{A}_r$, respectively. Then, the nonlinear system can be written as:

$$ {}^{t}\mathbf{A} = \begin{bmatrix} {}^{t}\mathbf{A}_p \\ {}^{t}\mathbf{A}_q \\ {}^{t}\mathbf{A}_r \end{bmatrix} = \mathbf{0} \tag{37} $$

where ${}^{t}\mathbf{A} \equiv {}^{t}\mathbf{A}(\mathbf{a})$, which is a function of the vector ${}^{t}\mathbf{a}$ containing the generalized coefficients, i.e. ${}^{t}\mathbf{a} = \left[{}^{t}\mathbf{a}^{\psi} \quad {}^{t}\mathbf{a}^{T} \quad {}^{t}\mathbf{a}^{C} \right]^{\mathrm{T}}$; the components of ${}^{t}\mathbf{a}^{\psi}$, ${}^{t}\mathbf{a}^{T}$, and ${}^{t}\mathbf{a}^{C}$, are a_I^{ψ}, a_I^{T}, and a_I^{C} for $I = 1,2,...,N_s$.

For computational efficiency, a two-step version of Newton-Raphson method is adopted [16] to solve the nonlinear system in Eq. (37). At time step t, the following equation is solved for the kth iterative step:

$$ {}^{t}_{k}\mathbf{J}\Delta\left({}^{t}_{k}\mathbf{a}\right) = -{}^{t}_{k}\mathbf{A} \tag{38} $$

in which

$$ {}^{t}_{k}\mathbf{J} = \begin{bmatrix} {}^{t}_{k}\mathbf{J}_p \\ {}^{t}_{k}\mathbf{J}_q \\ {}^{t}_{k}\mathbf{J}_r \end{bmatrix} \tag{39} $$

with

$$ {}^{t}_{k}\mathbf{J}_p = \begin{bmatrix} \dfrac{\partial\left({}^{t}_{k}\mathbf{A}_p^{\psi}\right)}{\partial\left({}^{t}_{k}\mathbf{a}^{\psi}\right)} & \dfrac{\partial\left({}^{t}_{k}\mathbf{A}_p^{\psi}\right)}{\partial\left({}^{t}_{k}\mathbf{a}^{T}\right)} & \dfrac{\partial\left({}^{t}_{k}\mathbf{A}_p^{\psi}\right)}{\partial\left({}^{t}_{k}\mathbf{a}^{C}\right)} \\ \dfrac{\partial\left({}^{t}_{k}\mathbf{A}_p^{T}\right)}{\partial\left({}^{t}_{k}\mathbf{a}^{\psi}\right)} & \dfrac{\partial\left({}^{t}_{k}\mathbf{A}_p^{T}\right)}{\partial\left({}^{t}_{k}\mathbf{a}^{T}\right)} & \dfrac{\partial\left({}^{t}_{k}\mathbf{A}_p^{T}\right)}{\partial\left({}^{t}_{k}\mathbf{a}^{C}\right)} \\ \dfrac{\partial\left({}^{t}_{k}\mathbf{A}_p^{C}\right)}{\partial\left({}^{t}_{k}\mathbf{a}^{\psi}\right)} & \dfrac{\partial\left({}^{t}_{k}\mathbf{A}_p^{C}\right)}{\partial\left({}^{t}_{k}\mathbf{a}^{T}\right)} & \dfrac{\partial\left({}^{t}_{k}\mathbf{A}_p^{C}\right)}{\partial\left({}^{t}_{k}\mathbf{a}^{C}\right)} \end{bmatrix} \tag{40} $$

$$ {}^{t}_{k}\mathbf{J}_q = \begin{bmatrix} \dfrac{\partial\left({}^{t}_{k}\mathbf{A}_q^{\psi}\right)}{\partial\left({}^{t}_{k}\mathbf{a}^{\psi}\right)} & \dfrac{\partial\left({}^{t}_{k}\mathbf{A}_q^{\psi}\right)}{\partial\left({}^{t}_{k}\mathbf{a}^{T}\right)} & \dfrac{\partial\left({}^{t}_{k}\mathbf{A}_q^{\psi}\right)}{\partial\left({}^{t}_{k}\mathbf{a}^{C}\right)} \\ \dfrac{\partial\left({}^{t}_{k}\mathbf{A}_q^{T}\right)}{\partial\left({}^{t}_{k}\mathbf{a}^{\psi}\right)} & \dfrac{\partial\left({}^{t}_{k}\mathbf{A}_q^{T}\right)}{\partial\left({}^{t}_{k}\mathbf{a}^{T}\right)} & \dfrac{\partial\left({}^{t}_{k}\mathbf{A}_q^{T}\right)}{\partial\left({}^{t}_{k}\mathbf{a}^{C}\right)} \\ \dfrac{\partial\left({}^{t}_{k}\mathbf{A}_q^{C}\right)}{\partial\left({}^{t}_{k}\mathbf{a}^{\psi}\right)} & \dfrac{\partial\left({}^{t}_{k}\mathbf{A}_q^{C}\right)}{\partial\left({}^{t}_{k}\mathbf{a}^{T}\right)} & \dfrac{\partial\left({}^{t}_{k}\mathbf{A}_q^{C}\right)}{\partial\left({}^{t}_{k}\mathbf{a}^{C}\right)} \end{bmatrix} \tag{41} $$

$$ {}^{t}_{k}\mathbf{J}_r = \begin{bmatrix} \dfrac{\partial\left({}^{t}_{k}\mathbf{A}_r^{\psi}\right)}{\partial\left({}^{t}_{k}\mathbf{a}^{\psi}\right)} & \dfrac{\partial\left({}^{t}_{k}\mathbf{A}_r^{\psi}\right)}{\partial\left({}^{t}_{k}\mathbf{a}^{T}\right)} & \dfrac{\partial\left({}^{t}_{k}\mathbf{A}_r^{\psi}\right)}{\partial\left({}^{t}_{k}\mathbf{a}^{C}\right)} \\ \dfrac{\partial\left({}^{t}_{k}\mathbf{A}_r^{T}\right)}{\partial\left({}^{t}_{k}\mathbf{a}^{\psi}\right)} & \dfrac{\partial\left({}^{t}_{k}\mathbf{A}_r^{T}\right)}{\partial\left({}^{t}_{k}\mathbf{a}^{T}\right)} & \dfrac{\partial\left({}^{t}_{k}\mathbf{A}_r^{T}\right)}{\partial\left({}^{t}_{k}\mathbf{a}^{C}\right)} \\ \dfrac{\partial\left({}^{t}_{k}\mathbf{A}_r^{C}\right)}{\partial\left({}^{t}_{k}\mathbf{a}^{\psi}\right)} & \dfrac{\partial\left({}^{t}_{k}\mathbf{A}_r^{C}\right)}{\partial\left({}^{t}_{k}\mathbf{a}^{T}\right)} & \dfrac{\partial\left({}^{t}_{k}\mathbf{A}_r^{C}\right)}{\partial\left({}^{t}_{k}\mathbf{a}^{C}\right)} \end{bmatrix} \tag{42} $$

where ${}^{t}_{k}\mathbf{J}$ represents the Jacobian matrix of ${}^{t}_{k}\mathbf{A}$. By using RKCM, ${}^{t}_{k}\mathbf{J}$ is a sparse matrix. $\Delta({}^{t}_{k}\mathbf{a})$ represents the increment of the vector of generalized coefficients. For the (k+1)th iterative step at time t, the vector of generalized coefficients cab be obtained by:

$$ {}^{t}_{k+1}\mathbf{a} = {}^{t}_{k}\mathbf{a} + \Delta\left({}^{t}_{k}\mathbf{a}\right) \tag{43} $$

from which the three variables can be calculated as:

$$ \begin{aligned} {}^{t}_{k+1}\psi(\mathbf{x}) &= \mathbf{\Psi}^{\mathrm{T}}(\mathbf{x})\,{}^{t}_{k+1}\mathbf{a}^{\psi} \\ {}^{t}_{k+1}T(\mathbf{x}) &= \mathbf{\Psi}^{\mathrm{T}}(\mathbf{x})\,{}^{t}_{k+1}\mathbf{a}^{T} \\ {}^{t}_{k+1}C(\mathbf{x}) &= \mathbf{\Psi}^{\mathrm{T}}(\mathbf{x})\,{}^{t}_{k+1}\mathbf{a}^{C} \end{aligned} \tag{44} $$

where

$$ \mathbf{\Psi}^{\mathrm{T}}(\mathbf{x}) = \begin{bmatrix} \Psi_1(\mathbf{x}) & \Psi_2(\mathbf{x}) & \cdots & \Psi_{N_s}(\mathbf{x}) \end{bmatrix} \tag{45} $$

In this study, the iteration at each time step t is implemented until $\max|\Delta({}^{t}_{k}\mathbf{a})| < 10^{-9}$ is satisfied.

4. Numerical Examples

In this section, all examples are analyzed using Matlab R2020a in a computer equipped with Intel i7-12700 and 32GB RAM. Without loss of generality, the following setup is adopted, unless otherwise stated: The support size $a = 3h$ for all RK shape functions, and the same discretization for source points N_s and collocation points N_c. To ensure a determined system of collocation equations, the corner points of a parallelogram are imposed by only one boundary condition for each variable. For presentation purpose, the evaluation points for contour plots are set as $N_e = (2N_{sx} - 1) \times (2N_{sy} - 1)$, with N_{sx} and N_{sy} denoting the numbers of source points in the x and y directions of the problem domain (i.e., $N_s = N_{sx} \times N_{sy}$). The following initial conditions are assumed: $a_I^T = 0$ and $a_I^C = 0$ (for $I = 1,2,...,N_s$).

Table 1. The iteration errors and condition numbers for various N_s (combined BCs).

N_s	41×41	61×61	81×81
Condition number	2.5110×10^5	6.6485×10^5	1.3454×10^6
CPU time (sec.)	29.1019	218.2969	1053.2289
No. of iteration	7	7	7

Table 2. Comparison of *Nu* and *Sh* with reference results (combined BCs).

Method		Present		Yang and Chang [18]		Li et al. [19]		Trevisan and Bejan [27]	
Ra	*Le*	*Nu*	*Sh*	*Nu*	*Sh*	*Nu*	*Sh*	*Nu*	*Sh*
100	1	3.15	3.15	3.15	3.15	3.13	3.13	-	-
	10	3.15	14.68	3.15	14.68	3.13	14.67	3.27	15.61
	20	3.15	21.35	3.15	21.35	3.13	22.14	-	-
200	1	5.13	5.13	5.13	5.13	5.09	5.09	-	-
	10	5.13	22.09	5.13	22.09	5.09	23.48	5.61	23.23
	20	5.13	30.41	5.13	30.41	5.09	35.09	-	-

Table 3. Comparison of *Nu* and *Sh* obtained by different N_c (combined BCs).

N_c		81×81		161×161		242×242	
Ra	*Le*	*Nu*	*Sh*	*Nu*	*Sh*	*Nu*	*Sh*
100	1	3.1477	3.1477	3.1477	3.1477	3.1477	3.1477
	10	3.1477	14.6831	3.1477	14.6828	3.1477	14.6827
	20	3.1477	21.3462	3.1477	21.3461	3.1477	21.3460
200	1	5.1311	5.1311	5.1310	5.1310	5.1309	5.1309
	10	5.1311	22.0901	5.1310	22.0900	5.1309	22.0899
	20	5.1310	30.4066	5.1310	30.4070	5.1309	30.4071
500	1	9.5819	9.5819	9.5815	9.5815	9.5814	9.5814
	10	9.5819	33.9138	9.5815	33.9144	9.5814	33.9144
	20	9.5819	43.0983	9.5815	43.0995	9.5814	43.0997
1000	1	14.6284	14.6284	14.6278	14.6278	14.6276	14.6276
	10	14.6284	43.5245	14.6278	43.5255	14.6276	43.5257
	20	14.6284	51.8105	14.6278	51.8119	14.6276	51.8122

4.1. Combined global heat and mass flows in a square

The boundary conditions (BCs) given in Eq. (16) and Eq. (18) for combined global heat and mass flows are considered in this example. The following parameters are adopted: $L = H = 1$, $Ra = 100$, $Le = 20$, and $N = 0$.

For various source points $N_s = 41\times41, 61\times61, 81\times81$, the convergence paths expressed in terms of the numbers of iteration are depicted in Fig. 2; the corresponding condition numbers and CPU time are summarized in Table 1. A stable and well-conditioned system is formed for each discretization, and the CPU time increases with respect to the number of source points. The steady-state results of ψ, T, and C obtained by $N_s = 81\times81$ are shown in Fig. 3, from which highly nonlinear behavior of C is exhibited. To further verify the results, the values of Nu and Sh obtained by different methods for various Ra and Le are compared in Table 2, where the present unsteady-state framework uses $N_s = 81\times81$, the steady-state framework of RKCM [18] uses $N_s = 81\times81$, and the space-time generalized finite difference method (ST-GFDM) [19] uses $N_s = 101\times101$ and $N_c = 5N_s$; another reference results are provided as well [27]. By observation, the desired accuracy is achieved by using RKCM for both unsteady-state and steady-state frameworks while less source points are adopted; in other words, higher computational efficiency is observed by the present method. Lastly, $N_s = 81\times81$ with different N_c is considered, and the results are listed in Table 3. With the increase in the number of N_c, both values of Nu and Sh get closer to the references; the variation in the values of these two parameters agrees well with literature [19], and the correctness of the results is ensured.

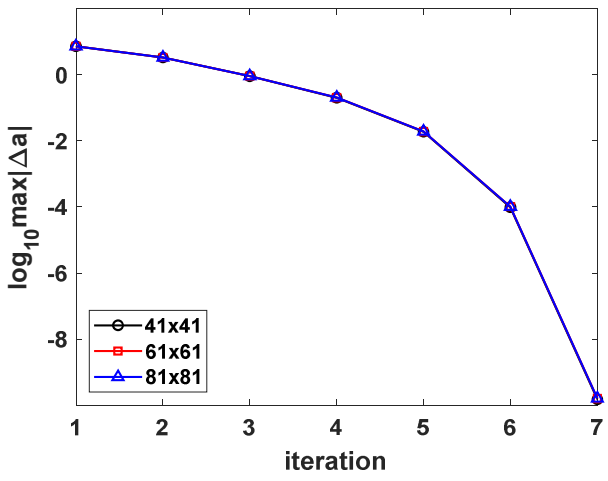

Fig. 2. Paths of convergence by various N_s for combined BCs.

4.2. Opposite global heat and mass flows in a square

The boundary conditions given in Eq. (17) and Eq. (18) for opposite global heat and mass flows are considered. The following parameters are adopted: $L = H = 1$, $Ra = 100$, $Le = 20$, and $N = 0$.

For $N_s = 41\times41, 61\times61, 81\times81$, the condition numbers, CPU time, and numbers of iteration are summarized in Table 4. In comparison with Table 1, it is observed that the two systems are numerically similar, including the condition numbers and computational time to solve the problems. The corresponding convergent process of solutions by different discretization are exhibited in Fig. 4; it is observed that both ψ and T can be approximated nicely by various N_s while C can be approximated well by $N_s = 81\times81$ only. In comparison with Fig. 3, it is observed that Fig. 4 (a) and Fig. 4 (b) are almost the same as Fig. 3 (a) and Fig. 3 (b) while Fig. 4 (c) is different from Fig. 3 (c) due to the opposite boundary conditions of the concentration. As a careful examination, Fig. 5 shows the results obtained by $Ra = 500$, $Le = 20$, and $N_s = 81\times81$ for both boundary conditions; for larger Ra, the contour lines in the center regions of ψ, T, and C becomes flatter in comparison with Fig. 3 and Fig. 4; moreover, the distribution of C reverses in terms of the magnitude for these two different boundary conditions, indicating that the concentration is arranged in the reverse direction while the recirculation is kept clockwise-rotating. The values of Nu and Sh computed by using both unsteady-state framework and steady-state framework [18] with $N_s = 81\times81$ are listed in Table 5, from which the numerical results are further confirmed.

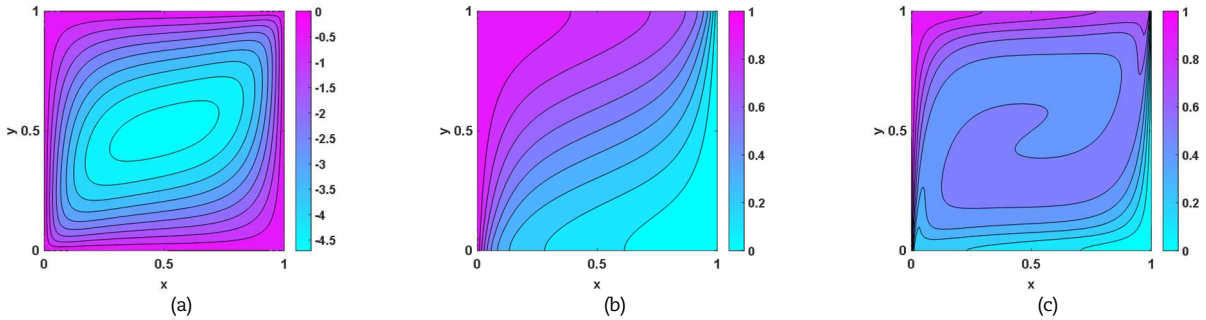

Fig. 3. Contour plots obtained by $N_s = 81\times81$ for combined BCs ($Ra = 100$ and $Le = 20$) (a) ψ; (b) T; ; (c) C.

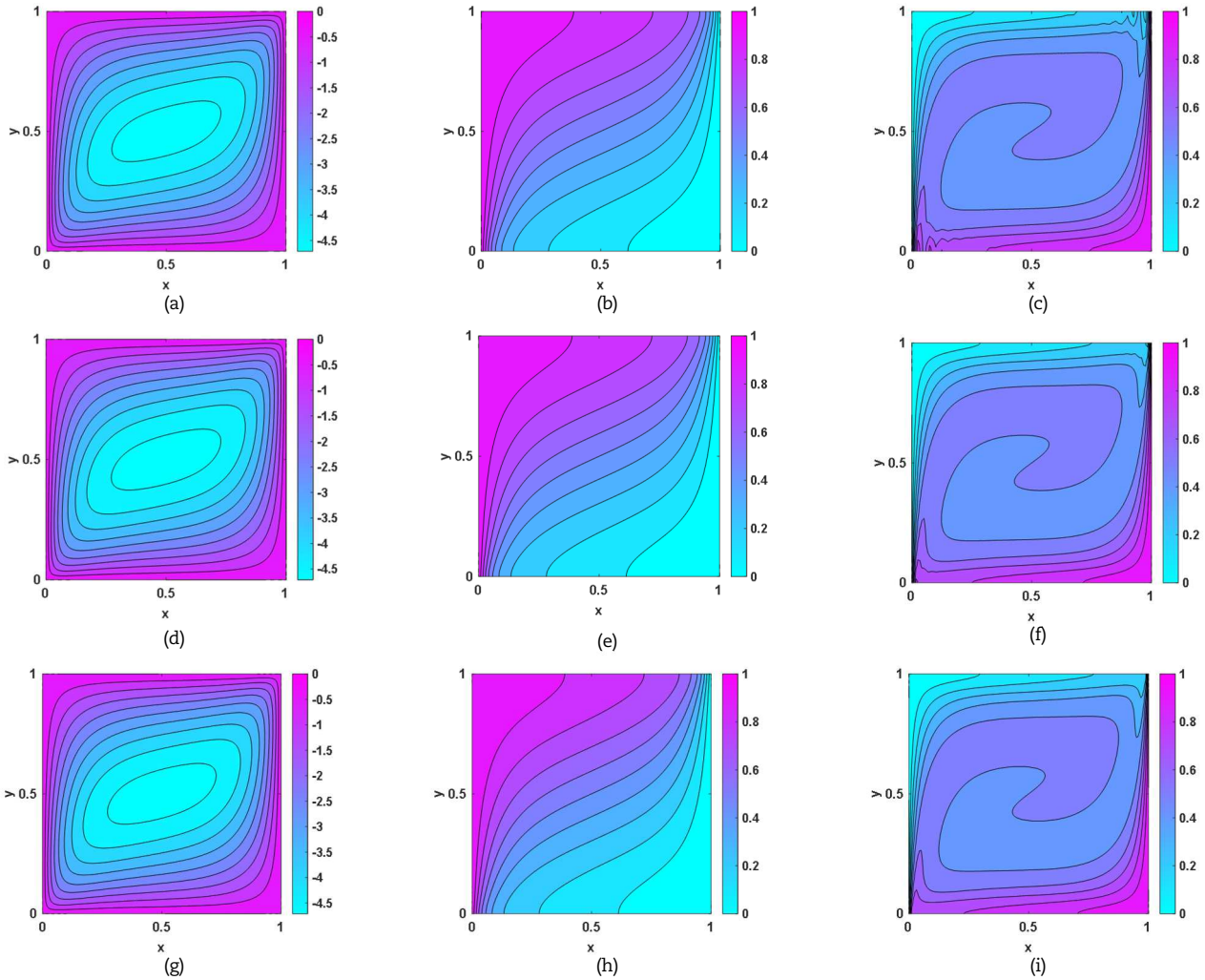

Fig. 4. Contour plots obtained by various N_s for opposite BCs ($Ra = 100$ and $Le = 20$) : (a)-(c) are ψ, T, and C by $N_s = 41\times41$; (d)-(f) are ψ, T, and C by $N_s = 61\times61$; (g)-(i) are ψ, T, and C by $N_s = 81\times81$.

Table 4. The iteration errors and condition numbers for various N_s (opposite BCs).

N_s	41×41	61×61	81×81
Condition number	2.5110×10^5	6.6485×10^5	1.3454×10^6
CPU time (sec.)	28.9656	223.0143	1097.5630
No. of iteration	7	7	7

Table 5. Comparison of *Nu* and *Sh* with reference results (opposite BCs).

Method		Present		Yang and Chang [18]	
Ra	*Le*	*Nu*	*Sh*	*Nu*	*Sh*
100	1	3.15	3.15	3.15	3.15
	10	3.15	14.68	3.15	14.68
	20	3.15	21.35	3.15	21.35
200	1	5.13	5.13	5.13	5.13
	10	5.13	22.09	5.13	22.09
	20	5.13	30.41	5.13	30.41

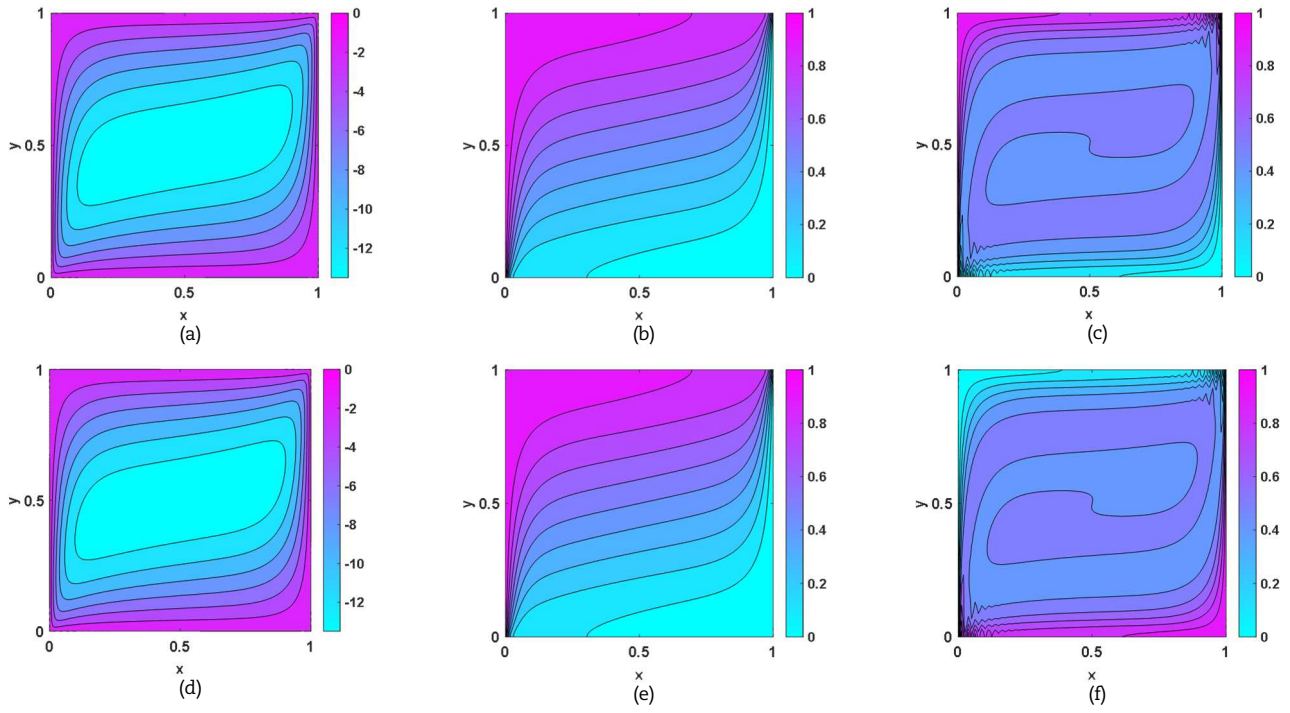

Fig. 5. Contour plots obtained by $N_s = 81\times81$ ($Ra = 500$ and $Le = 20$) : (a)-(c) present ψ, T, and C for combined BCs; (d)-(f) present ψ, T, and C for opposite BCs.

4.3. Solute transferring problem in a parallelogram

For nonzero buoyancy ratio N, the nonlinear coupling of the system is enhanced, leading to a fully solute transferring problem. In this example, the full solute transferring problem in a parallelogram, as schematically shown in Fig. 6, is investigated. The boundary conditions of combined global heat and mass flows presented in Section 4.1 are adopted again; particularly, the boundary conditions of two inclined sides are given in Eq. (19). The formulae for computing the average parameters Nu and Sh in a parallelogram are modified as follows [21]:

$$Nu = \frac{1}{(H/L)\cos\theta}\int_0^H \left.\frac{\partial T}{\partial x}\right|_{x=0} dy \tag{46}$$

$$Sh = \frac{1}{(H/L)\cos\theta}\left|\int_0^H \left.\frac{\partial C}{\partial x}\right|_{x=0} dy\right| \tag{47}$$

where the inclined angle θ is defined as the angle measured from the horizontal x axis to the inclined side of parallelogram in the counterclockwise direction. The above equation applies to θ between -90° and 90°.

The following parameters are considered first: $L = H = 1$, $Ra = 100$, $Le = 0.8$, $N = 2$, and $-60^\circ \le \theta \le 60^\circ$. The results of Nu and Sh versus θ are respectively plotted in Fig. 7 (a) and (b), in which $N_s = 81\times81$ and $N_e = 81\times81$ are adopted herein. By comparison, both Nu and Sh agree well with the reference solutions [21], although there is some small discrepancy; this can be attributed to different numerical methods and discretization adopted in the analysis, i.e., FEM with non-uniform mesh in Ref. [21]. Besides, it is noticed that for Le and N close to unity in this example, the behaviors of T and C become similar as implied by Eqs. (12)-(14) and Eqs. (46)-(47), which further verify the results obtained by the present method. The viability of the proposed framework in solving the solute transferring problems is assured in concern of various geometric inclinations.

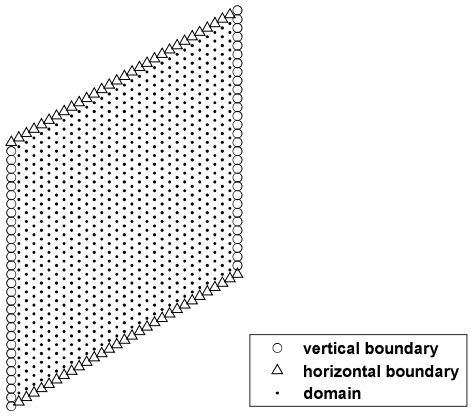

Fig. 6. The schematic layout of collocation points in a parallelogram.

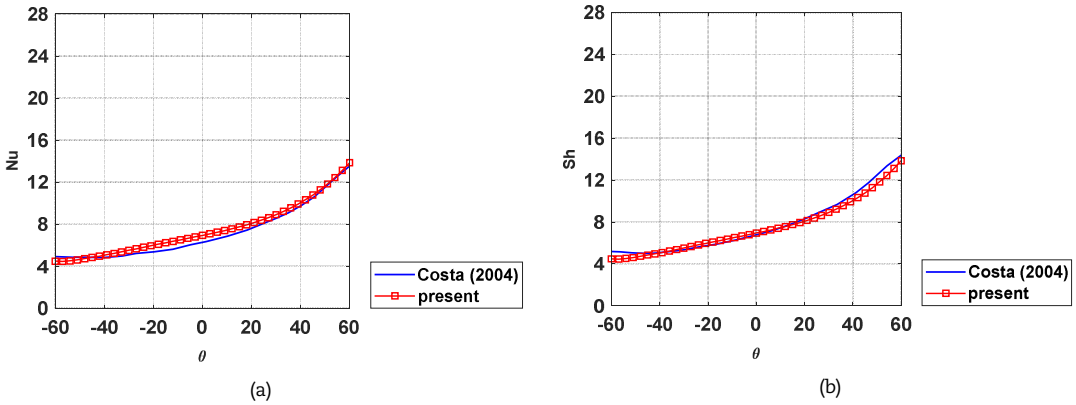

Fig. 7. The average parameters vs. the inclined angle θ : (a) Nu; (b) Sh.

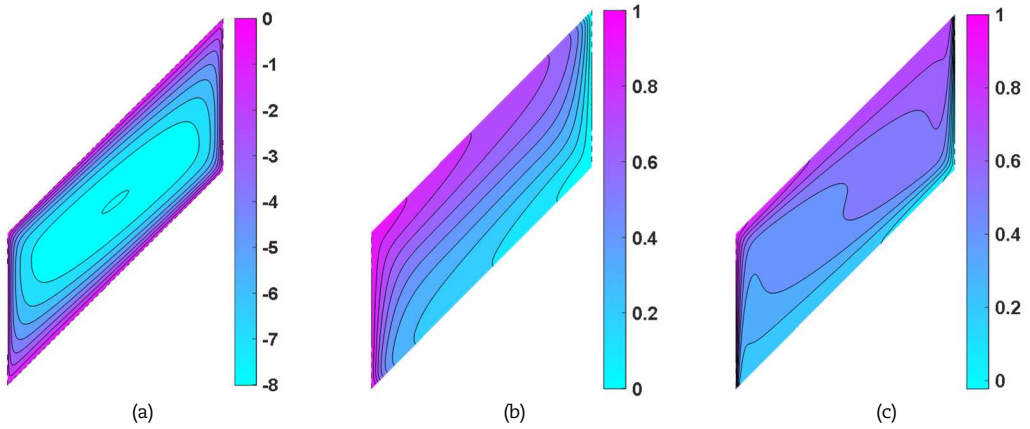

Fig. 8. Contour plots obtained by $N_s = 31 \times 91$ for combined BCs ($Ra = 100$, $Le = 8$, and $N = 2$) : (a) ψ; (b) T; (c) C.

Next, a parallelogram with $\theta = 45^\circ$ is considered, with the following parameters adopted: $L/H = 2$, $Ra = 100$, $Le = 8$, and $N = 2$. For this geometry, $N_s = 31 \times 91$ and $a = 2.8h$. The results of ψ, T, and C are shown in Fig. 8. With the aid of more source points discretized on the longer side of the parallelogram, the contour plot of C near the corners still exhibits smooth approximation, even for such a large value of Le.

4.4. Monocellular natural/anti-natural flow in a square

A square domain $L = H = 1$ is considered herein. For the monocellular natural/anti-natural flow (MNF/MAF) problem, the imposition of heat source on the boundary is schematically illustrated in Fig. 9, with the following boundary conditions [24]:

For $x = 0$,

$$\psi(0,y) = 0,\ \frac{\partial T}{\partial x}(0,\ y) = 0,\ C(0,y) = 0 \tag{48}$$

For $x = 1$,

$$\psi(1,y) = 0,\ \frac{\partial T}{\partial x}(1,\ y) = 0,\ C(1,y) = 1 \tag{49}$$

For $y = 0$ and $0.5 \le x \le 1$,

$$\psi(x, 0) = 0,\ T(x, 0) = 1,\ \frac{\partial C}{\partial y}(x, 0) = 0 \tag{50}$$

For $y = 0$ and $0 < x < 0.5$,

$$\psi(x, 0) = 0,\ \frac{\partial T}{\partial y}(x, 0) = 0,\ \frac{\partial C}{\partial y}(x, 0) = 0 \tag{51}$$

For $y = 1$,

$$\psi(x, 1) = 0,\ T(x, 1) = 0,\ \frac{\partial C}{\partial y}(x, 1) = 0 \tag{52}$$

When the boundary is heated partially, the behavior of fluid changes according to the value of buoyancy ratio N. For $N > 0$, it leads to a monocellular natural flow; for $N < 0$, it is monocellular anti-natural flow. In this example, $Ra = 100$, $Le = 1$, and $N_s = 81 \times 81$. By using $N = 10$, the results of ψ, T, and C are shown in Fig. 10; the cell rotation is counter-clockwise as shown in the stream function, while the regular pattern (e.g. in the previous examples) is no longer available for the temperature field due to the asymmetric nature of heat source. For $N = -10$, the results of ψ, T, and C are shown in Fig. 11, in which the cell rotation is in the reverse direciton for the stream function. By comparing Fig. 10 with Fig. 11, both the contours of ψ and C exhibit opposite behaviors; for MNF, the fluid is governed by the buoyancy force due to the temperature, thereby making the contour of T distribute vertically from the heat source over the right part of the domain; for MAF, the fluid is under the control of the buoyancy force due to the concentration, thereby making the contour of T diffuse vertically over the left part of the domain. Furthermore, as the thermal buoyancy force generated by the heat source tends to resist the solute buoyancy force (the governor in this case) when $N < 0$, the monocellular anti-natural flow requires more iteration.

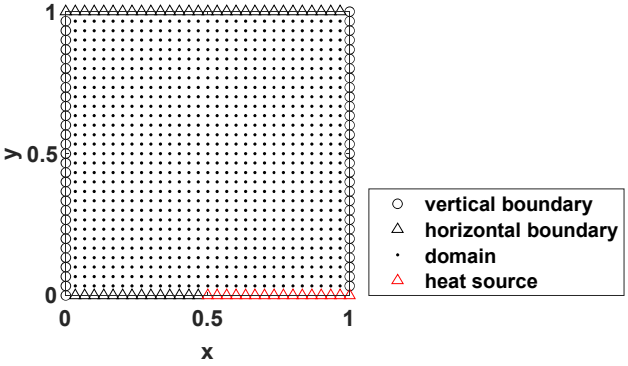

Fig. 9. The schematic layout of collocation points in a square.

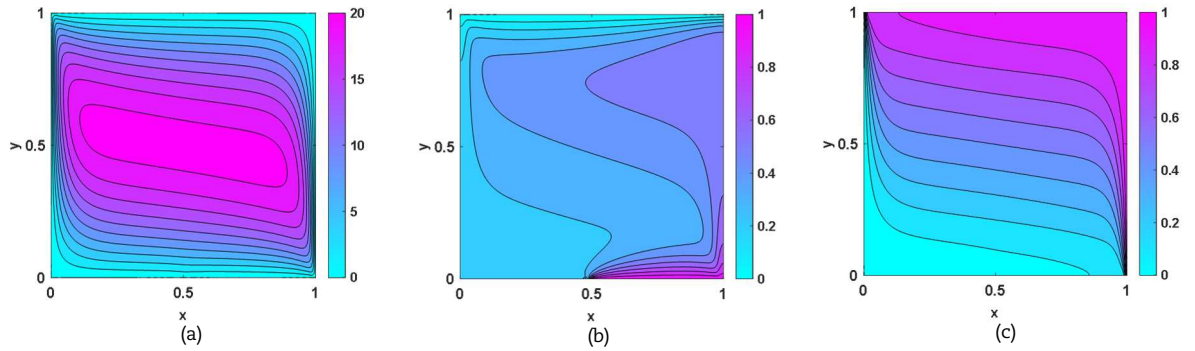

Fig. 10. Contour plots for monocellular natural flow: (a) ψ; (b) T; (c) C.

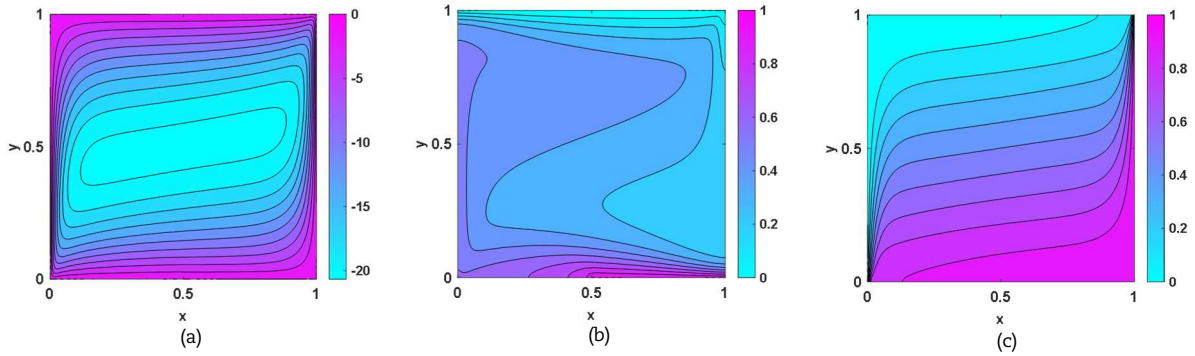

Fig. 11. Contour plots for monocellular anti-natural flow: (a) ψ; (b) T; (c) C.

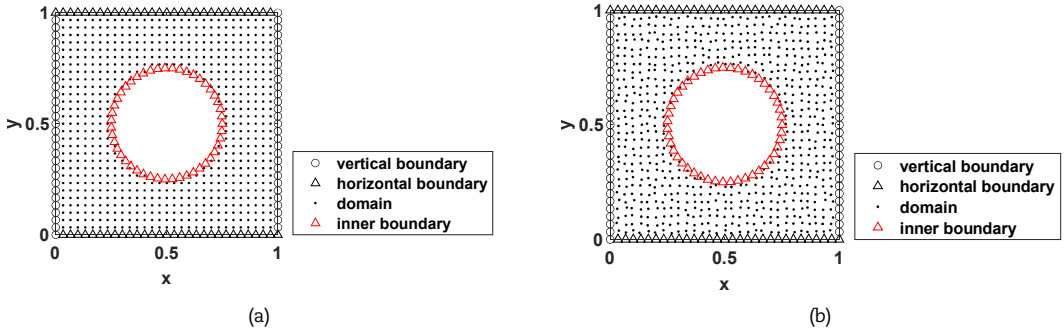

Fig. 12. The schematic layout of collocation points in simply connected domains: (a) uniform; (b) non-uniform.

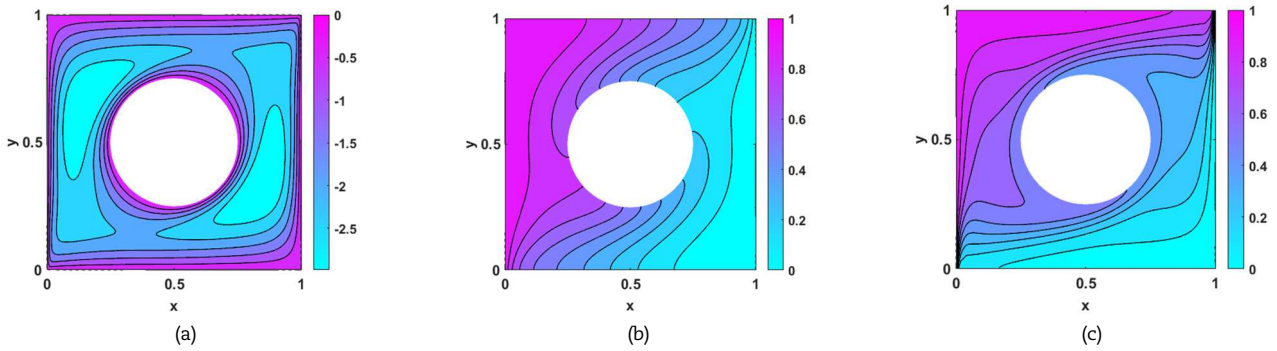

Fig. 13. Contour plots for simply connected domains (uniform discretization): (a) ψ; (b) T; (c) C.

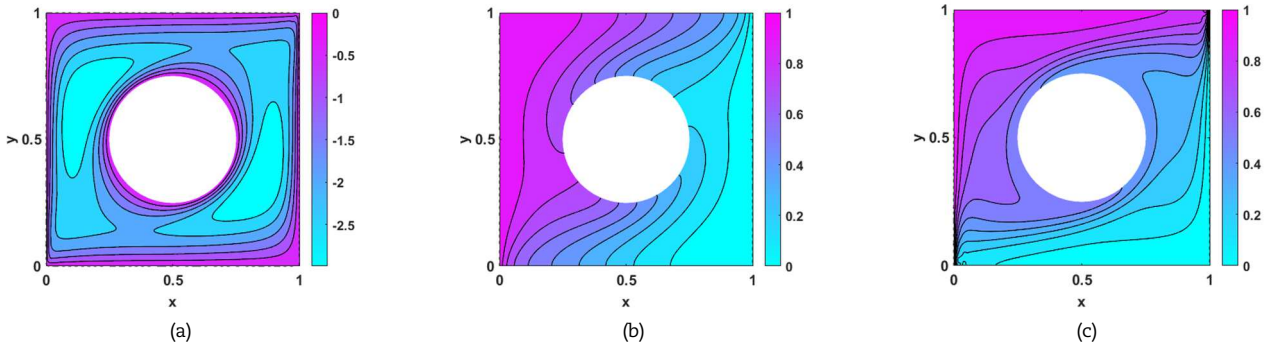

Fig. 14. Contour plots for simply connected domains (non-uniform discretization): (a) ψ; (b) T; (c) C.

4.5. Simply connected and multiply connected domains

To explore the meshfree nature of the numerical framework, both uniform discretization and non-uniform discretization are considered; additionally, both simply and multiply connected domains are included as motivated by the previous studies [28, 29]. The following equations are adopted for generating the coordinates (x,y) in the non-uniform discretization:

$$x = x + \frac{s}{10}(-1+2rand)h$$
$$y = y + \frac{s}{10}(-1+2rand)h \tag{53}$$

where s denotes the disturbance of coordinate, and $rand = rand(1)$ denotes a random numebr between 0 and 1 in Matlab. In this example, $s = 2$ is adopted, which indicates that the disturbance could cause the deviation of a point within 20% of the original coordinate.

The following parameters are assumed: $L = H = 1$, $Ra = 100$, $Le = 8$, $N = 2$, an inner radius of $r = 0.25$ for the hole in the simply connected domain, and an inner radius of $r = 0.15$ for the two holes in the multiply connected domain. The boundary conditions given in Eq. (16) and Eq. (18) are assumed for the outer boundary; the inner boundary is assumed to be impermeable ($\psi = 0$) without diffusion of heat and mass [19], as described by Eq. (19). To reach smooth streamline, $a = 3.5h$ is adopted for both simply and multiply connected domains.

As shown in Fig. 12 (a) and (b), the uniform discretization and non-uniform discretization of simply connected domains are based on 81×81 points discretized in the background square, and $N_s = 5432$ after the removal of points in the hole. For uniform and non-uniform discretization, Fig. 13 and Fig. 14, respectively exhibit the corresponding contour plots, from which the patterns of anti-symmetry are observed for the streamline of ψ, T, and C, and both discretization yield similar results with desired accuracy. Table 6 summarizes the information of the two systems during nonlinear analysis; it is found that the non-uniform discretization requires more time to converge while the rest results are similar to those of uniform discretization. For the simply connected domain, the contours of ψ and T along the hole exhibit similar distribution (in terms of values) to those on the top and bottom boundary; the flow of ψ separates into two vortexes while the flow of C rotates along the hole.

Table 6. Information of simply connected problems.

Discretization	Uniform	Non-uniform
Condition number	6.9262×10^6	2.9194×10^6
CPU time (sec.)	558.8040	566.3812
No. of iteration	8	8

Table 7. Information of multiply connected problems.

Discretization	Uniform	Non-uniform
Condition number	1.1941×10^6	1.8978×10^6
CPU time (sec.)	767.0183	773.3465
No. of iteration	9	9

The multiply connected domains with uniform and non-uniform discretization are shown in Fig. 15 (a) and (b), where $N_s = 5829$ on the basis of 81×81 points discretized in the background square. As shown in Fig. 16 and Fig. 17, the anti-symmetric patterns of streamline for ψ, T, and C are observed again for both discretization, regardless of the number of holes in the domain; in Fig. 17(c), some tiny oscillations are observed in the top right and bottom left corners. Table 7 displays the convergence information of the two systems, from which it is observed that the non-uniform discretization leads to a less stable system for the current subject in consideration. For the multiply connected domain, the contour of T along the two holes exhibits similar distribution (in terms of values) to those on the top and bottom boundary again; the flow of C rotates along the two holes; the flow of ψ is compressed by the geometry of two holes such that the two vortexes are not fully separated.

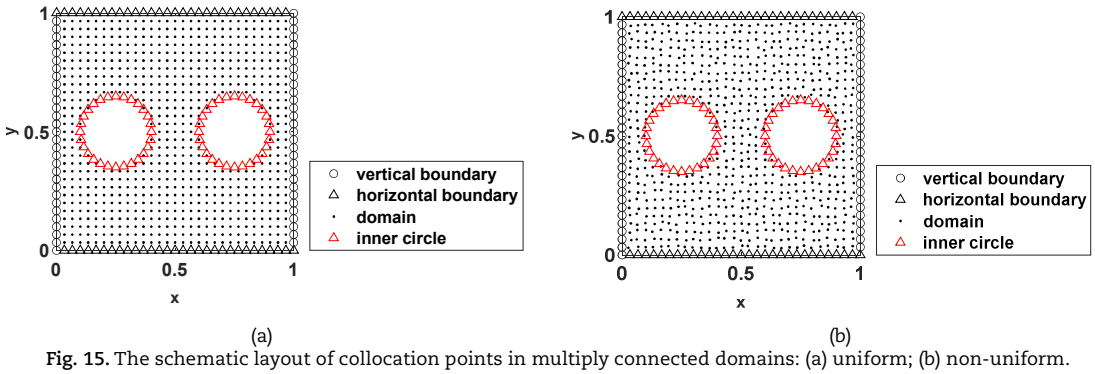

Fig. 15. The schematic layout of collocation points in multiply connected domains: (a) uniform; (b) non-uniform.

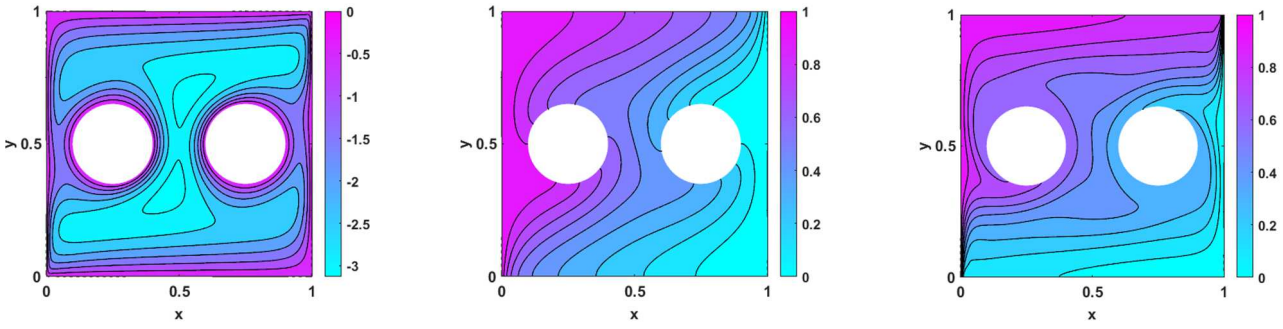

Fig. 16. Contour plots for multiply connected domains (uniform discretization): (a) ψ; (b) T; (c) C.

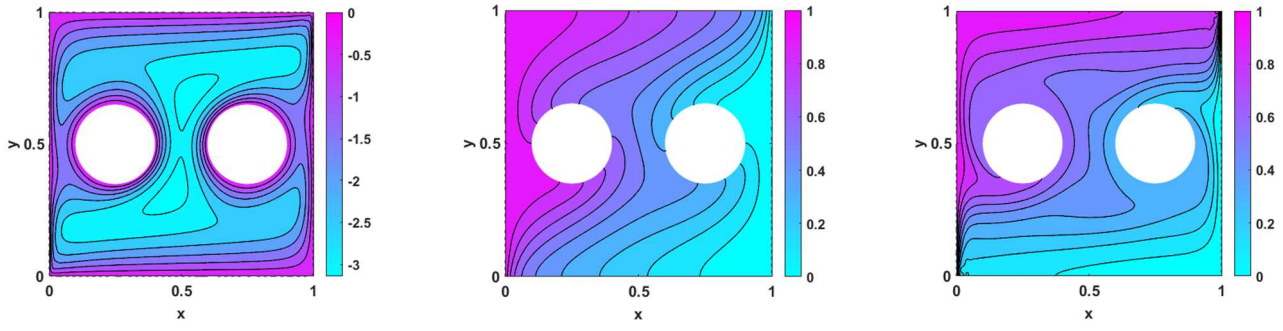

Fig. 17. Contour plots for multiply connected domains (non-uniform discretization): (a) ψ; (b) T; (c) C.

5. Conclusion

In this study, the unsteady meshfree framework based on RKCM for nonlinear analysis of porous enclosures is established to solve three-phase coupling problems. To ensure the computational efficiency, the corner points on the domain boundary are imposed by one boundary condition for each variable such that a determined and well-conditioned system can be reached. The flexibility of meshfree nature is validated through complex geometry of connected domains and non-uniform discretization. The numerical results show that the buoyancy force governs the behaviors of the field variables under the partially heated boundary, especially for the distribution pattern of temperature. Concerning the geometric effects of the hole(s) in the domains, various vortexes might be formed and separated depending on the inner geometry. The numerical framework has been demonstrated to be stable and effective in retrieving the smooth contours for multi variables in concern of high nonlinearity by uniform discretization with few points in the approximation.

Author Contributions

J.P. Yang planned the scheme, examined the derivation, validated the results, and wrote the manuscript. I-.T. Liao derived the equations and conducted the numerical analysis. All authors discussed the results and approved the manuscript.

Acknowledgements

The authors would like to express our sincere thanks to the reviewers for the constructive and valuable comments on this study.

Conflict of Interest

The authors declared no potential conflicts of interest concerning the research, authorship, and publication of this article.

Funding

The full support of this work under the grant number MOST 111-2628-E-A49-009-MY3 by National Science and Technology Council in Taiwan is acknowledged.

Data Availability Statements

No data were used in this study.

References

[1] Huppert, H. E., Turner, J. S., Double-diffusive convection, *Journal of Fluid Mechanics*, 106, 1981, 299-329.
[2] Nishimura, T., Wakamatsu, M., Morega, A. M., Oscillatory double-diffusive convection in a rectangular enclosure with combined horizontal temperature and concentration gradients, *International Journal of Heat and Mass Transfer*, 41(11), 1998, 1601-1611.
[3] Nield, D. A., Kuznetsov, A.V., The onset of double-diffusive convection in a nanofluid layer, *International Journal of Heat and Fluid Flow*, 32, 2011, 771-776.
[4] Maatki, C., Ghachem, K., Kolsi, L., Hussein, A. K., Borjini, M. N., Aissia, H. B., Inclination effects of magnetic field direction in 3D double-diffusive natural convection, *Applied Mathematics and Computation*, 273, 2016, 178-189.
[5] Chamkha, A. J., Double-diffusive natural convection in a porous enclosure with cooperating temperature and concentration gradients and heat generation or absorption effects, *Numerical Heat Transfer*, 47(12-13), 2002, 2699-2714.
[6] Yang, J. Q., Zhao, B. X., Numerical investigation of double-diffusive convection in rectangular cavities with different aspect ratio I: High-accuracy numerical method, *Computer and Mathematics with Applications*, 94, 2021, 155-169.
[7] Goyeau, B., Songbe, J.P., Gobin, D., Numerical study of double-diffusive natural convection in a porous cavity using the Darcy-Brinkman formulation, *International Journal of Heat and Mass Transfer*, 39, 1996, 1363-1378.
[8] Hasnaoui, S., Amahmid, A., Raji, A., Beji, H., Hasnaoui, M., Dahani, Y., Benhamed, H., Double diffusive natural convection in an inclined enclosure with heat generation and Soret effect, *Engineering Computations*, 35, 2018, 2753-2774.
[9] March, R., Coutinho, A. L.G.A., Elias, R. N., *Stabilized Finite Element Simulation of Double Diffusive Natural Convection*, Mecánica Computacional, Buenos Aires, Argentina, 2010.
[10] Hao, Y., Nitao, J., Buscheck, T. A., Sun, Y., Double diffusive natural convection in a nuclear waste repository, *International High-Level Radioactive Waste Management Conference*, Las Vegas, United States, 2006.
[11] Wang, D., Wang, J., Wu, J., Arbitrary order recursive formulation of meshfree gradients with application to superconvergent collocation analysis of Kirchhoff plates, *Computational Mechanics*, 65, 2020, 877-903.
[12] Wang, L., Qian, Z., A meshfree stabilized collocation method (SCM) based on reproducing kernel approximation, *Computer Methods in Applied Mechanics and Engineering*, 371, 2020, 113303.
[13] Yang, J. P., Lin, Q., Investigation of multiply connected inverse Cauchy problems by efficient weighted collocation method, *International Journal of Applied Mechanics*, 12(1), 2020, 2050012.
[14] Yang, J. P., Li, H. M., Recovering heat source from fourth-order inverse problems by weighted gradient collocation, *Mathematics*, 10(2), 2022, 241.
[15] Fan, C. M., Chien, C. S., Chan, H. F., Chiu, C. L., The local RBF collocation method for solving the double-diffusive natural convection in fluid-saturated porous media, *International Journal of Heat and Mass Transfer*, 57, 2013, 500-503.
[16] Li, P. W., Chen, W., Fu, Z. J., Fan, C. M., Generalized finite difference method for solving the double-diffusive natural convection in fluid-saturated porous media, *Engineering Analysis with Boundary Elements*, 95, 2018, 175-186.
[17] Yang, J. P., Liao, Y. S., Direct collocation with reproducing kernel approximation for two-phase coupling system in a porous enclosure, *Mathematics*, 9(8), 2021, 897.
[18] Yang, J. P., Chang, H. C., Meshfree collocation method for double-diffusive natural convection in a porous enclosure using reproducing kernel approximation, *Journal of Thermal Stresses*, 2023, accepted.
[19] Li, P. W., Grabski, J. K., Fan, C. M., Wang, F., A space-time generalized finite difference method for solving unsteady double-diffusive natural convection in fluid-saturated porous media, *Engineering Analysis with Boundary Elements*, 142, 2022, 138-152.
[20] Yang, J. P., Chang, H. C., Meshfree collocation framework for multi-phase coupling nonlinear dynamic system in a porous enclosure, *International Journal of Structural Stability and Dynamic*, 22(15), 2022, 2271004.
[21] Costa, V. A. F., Double-diffusive natural convection in parallelogrammic enclosures filled with fluid-saturated porous media, *International Journal of*

Heat and Mass Transfer, 47, 2004, 2699-2714.
[22] Shiina, Y., Hishida, M., Critical Rayleigh number of natural convection in high porosity anisotropic horizontal porous layers, *International Journal of Heat and Mass Transfer*, 53(7-8), 2010, 1507-1513.
[23] Bilal Ashraf, M., Hayat, T., Alsaedi, A., Shehzad, S. A., Soret and Dufour effects on the mixed convection flow of an Oldroyd-B fluid with convective boundary conditions, *Results in Physics*, 6, 2016, 917-924.
[24] Bourich, M., Hasnaoui, M., Amahmid, A., Double-diffusive natural convection in a porous enclosure partially heated from below and differentially salted, *International Journal of Heat and Fluid Flow*, 24, 2004, 1034-1046.
[25] Wang, D., Wang, J., Wu, J., Superconvergent gradient smoothing meshfree collocation method, *Computer Methods in Applied Mechanics and Engineering*, 340, 2018, 728-766.
[26] Deng, L., Wang, D., An accuracy analysis framework for meshfree collocation methods with particular emphasis on boundary effects, *Computer Methods in Applied Mechanics and Engineering*, 404, 2023, 115782.
[27] Trevisan, O. V., Bejan, A., Natural convection with combined heat and mass transfer buoyancy effects in a porous medium, *International Journal of Heat and Mass Transfer*, 28, 1985, 1597-1611.
[28] Yang, J. P., Lin, Q., Investigation of multiply connected inverse Cauchy problems by efficient weighted collocation method, *International Journal of Applied Mechanics*, 12(1), 2020, 2050012.
[29] Yang, J. P., Lam, H. F. S., Detecting inverse boundaries by weighted high-order gradient collocation method, *Mathematics*, 8(8), 2020, 1297.

ORCID iD

Judy P. Yang https://orcid.org/0000-0002-3792-2821
I-Ting Liao https://orcid.org/0009-0005-5541-992X

How to cite this article: Yang J.P., Liao I.T. Unsteady Meshfree Framework for Double-diffusive Natural Convection with Boundary and Geometry Effects, *J. Appl. Comput. Mech.*, 10(2), 2024, 272–286. https://doi.org/10.22055/jacm.2023.44690.4259